Designed nanomolar small-molecule inhibitors of Ena/VASP EVH1 interaction impair invasion and extravasation of breast cancer cells

Barone, M.; Muller, M.; Chiha, S.; Ren, J.; Albat, D.; Soicke, A.; ... ; Kuhne, R.

Designed nanomolar small-molecule inhibitors of Ena/VASP EVH1 interaction impair invasion and extravasation of breast cancer cells

Matthias Barone[a] , Matthias Müller[a], Slim Chiha[b], Jiang Ren[c], Dominik Albat[b], Arne Soicke[b], Stephan Dohmen[b], Marco Klein[b], Judith Bruns[b], Maarten van Dinther[c], Robert Opitz[a], Peter Lindemann[a], Monika Beerbaum[a], Kathrin Motzny[a], Yvette Roske[d], Peter Schmieder[a] , Rudolf Volkmer[a], Marc Nazaré[a] , Udo Heinemann[d,e] , Hartmut Oschkinat[a,e], Peter ten Dijke[c,1], Hans-Günther Schmalz[b,1] , and Ronald Kühne[a,1]

[a]Department of Structural Biology, Leibniz-Forschungsinstitut für Molekulare Pharmakologie, 13125 Berlin, Germany; [b]Department of Chemistry, Universität zu Köln, 50939 Köln, Germany; [c]Oncode Institute, Department of Cell and Chemical Biology, Leiden University Medical Center, 2333 Leiden, The Netherlands; [d]Department of Macromolecular Structure and Interaction, Max-Delbrück-Centrum für Molekulare Medizin, 13125 Berlin, Germany; and [e]Institute of Chemistry and Biochemistry, Freie Universität Berlin, 14195 Berlin, Germany

Battling metastasis through inhibition of cell motility is considered a promising approach to support cancer therapies. In this context, Ena/VASP-depending signaling pathways, in particular interactions with their EVH1 domains, are promising targets for pharmaceutical intervention. However, protein–protein interactions involving proline-rich segments are notoriously difficult to address by small molecules. Hence, structure-based design efforts in combination with the chemical synthesis of additional molecular entities are required. Building on a previously developed nonpeptidic micromolar inhibitor, we determined 22 crystal structures of ENAH EVH1 in complex with inhibitors and rationally extended our library of conformationally defined proline-derived modules (ProMs) to succeed in developing a nanomolar inhibitor (K_d = 120 nM, MW = 734 Da). In contrast to the previous inhibitor, the optimized compounds reduced extravasation of invasive breast cancer cells in a zebrafish model. This study represents an example of successful, structure-guided development of low molecular weight inhibitors specifically and selectively addressing a proline-rich sequence-recognizing domain that is characterized by a shallow epitope lacking defined binding pockets. The evolved high-affinity inhibitor may now serve as a tool in validating the basic therapeutic concept, i.e., the suppression of cancer metastasis by inhibiting a crucial protein–protein interaction involved in actin filament processing and cell migration.

protein–protein interactions | metastasis | small molecules | peptide mimetics | proline-rich motif

Metastasis is a complex multistep process (1, 2) employing, among others, mechanisms governing actin cytoskeleton dynamics involving integrin signaling and actin regulatory proteins (3–5). So far, all approved antimetastatic drugs antagonize integrins (6) or inhibit downstream kinases (7, 8) (SI *Appendix,* Fig. S1). In the metastatic setting however, these drugs appear to have only limited success (9–13) and 5-y survival is not increasing satisfactorily (14, 15), making new approaches in antimetastatic drug development essential to meet this urgent medical need.

The enabled/vasodilator stimulated phosphoprotein protein family (Ena/VASP) acts as a crucial hub in cell migration by linking actin filaments to invadopodia and focal adhesions (16–22). Due to their role in the transformation of benign lesions into invasive and metastatic cancer, Ena/VASP proteins are discussed as part of the invasive signature and as a marker of breast carcinogenesis (23–25). At the advanced tumor stage, the protein family is overexpressed (26–28), which has been shown to increase migration speed in vivo (29) and to potentiate invasiveness (30). Yet, no sufficiently potent probes to interfere with Ena/VASP in vivo have been reported.

The three vertebrate Ena/VASP family members, enabled homolog (ENAH), VASP, and Ena-VASP-like (EVL), share a tripartite structural organization in which two Ena/VASP homology domains (EVH1 and EVH2) are separated by a more divergent proline-rich central part. Interactions of the EVH2 domain are involved in the elongation and protection of barbed-end actin filaments from capping proteins and tetramerization (31, 32). EVH1 folds into a structured globular domain that interacts with proteins at focal adhesions (33), the leading edge (34, 35), and invadopodia (36, 37) by recognizing the motif [F/W/L/Y]PxɸP (35, 38) (ɸ hydrophobic, x any; SI *Appendix,* Fig. S3) in poly-L-proline type II helix (PPII) conformation.

In the course of our research into small molecules as potential inhibitors of protein–protein interactions (39) we recently in silico designed and stereo-selectively synthesized scaffolds, coined ProMs, which mimic pairs of prolines in PPII conformation (40). The modular combination of different ProMs thereby allowed us to generate nonpeptidic secondary-structure mimetics that fulfill the steric requirements of the addressed proline-rich motif-recognizing domain (41–47). For the EVH1 domain, our proof-of-concept study yielded a canonically binding, nontoxic,

Significance

Protein–protein interactions mediated by proline-rich motifs are involved in regulation of many important signaling cascades. These motifs belong to the most abundant recognition motifs in the eukaryotic genome and preferentially adopt a left-handed polyproline helix II, a secondary structure element that has been notoriously difficult to mimic with small molecules. Here, we present a structure-guided design effort yielding a toolkit of chemical entities that enables rational construction of selective small molecule inhibitors for these protein domains. We succeeded in developing an inhibitor for the Ena/VASP protein family that is active in vivo and reduces extravasation of invasive breast cancer cells in a zebrafish model.

cell-membrane-permeable, 706-Da inhibitor **1** (Fig. 1*A*) composed of two different ProM scaffolds and 2-chloro-(*L*)-phenylalanine (2-Cl-Phe) (40). While the synthetic inhibitor **1** represents the compound with the highest reported affinity toward Ena/VASP EVH1 domains, a further improvement was required for in vivo experiments. Here we report successful structure-based optimization of inhibitor **1** based on 22 high-resolution crystal structures of ENAH EVH1 in complex with different inhibitors (*SI Appendix*, Tables S1–S6), including the well-resolved C-terminal binding epitope TEDEL of ActA from *Listeria monocytogenes* (48). Newly identified interaction sites adjacent to the C terminus of **1** were addressed by in silico designed and stereo-selectively synthesized modifications of the ProM-1 scaffold (Fig. 1*A*). While drastically increasing the affinity against a rather flat protein surface we conserved structural simplicity, low molecular weight, nontoxicity, and cell-membrane permeability. Potent compounds against Ena/VASP were shown to also act in vivo, i.e., by inhibiting cancer cell extravasation in zebrafish at only 1 μM, thereby paving the way for future preclinical studies.

Results

Synthesis and Characterization of Inhibitors. The compounds employed in this study were synthesized by modular assembly of the building blocks using established coupling protocols (40). The required ProM scaffolds ProM-1 (41, 43), ProM-2 (45), ProM-9 (46), ProM-13 (46), ProM-15 (47), and ProM-17 (47) (Fig. 1*B*) were synthesized as separately published. The binding of the inhibitors toward ENAH EVH1 was assessed by means of fluorescence titration as described in *SI Appendix*. The obtained K_d and the change of free energy upon binding (ΔG) are given in Table 1.

Initial Considerations. As mentioned above, inhibitor **1** served as the starting point for ligand optimization. It represents the pentapeptide core recognition motif **wt1** of the high-affinity
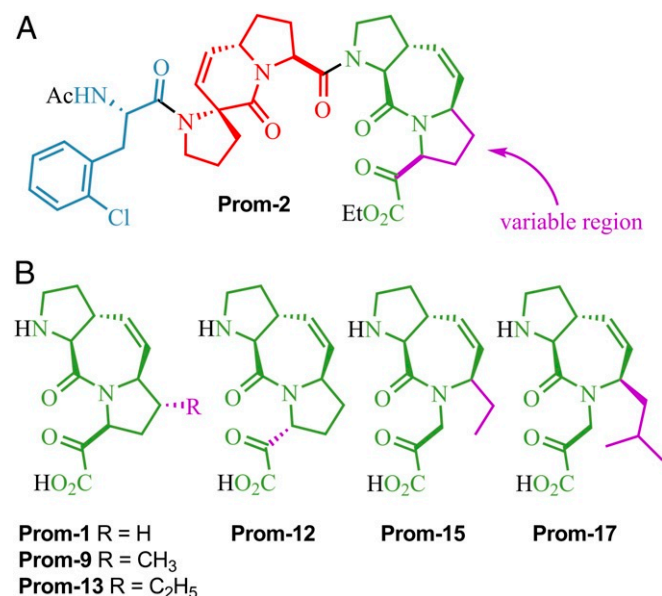

Fig. 1. (*A*) Structure of the first-generation Ena/VASP EVH1 inhibitor **1**. All compositions share the *N*-acetylated 2-chloro-phenylalanine unit (blue) attached to a central ProM-2 scaffold (red). Esterification of the C terminus renders the inhibitors cell-membrane permeable (40). (*B*) General (modular) architecture of nonpeptidic, conformationally preorganized inhibitors used in this study. Structural variation (pink) was achieved by replacing the C-terminal ProM-1 unit (green) by ProM-9, ProM-13, ProM-12, ProM-15, or ProM-17 (Table 1).

ActA-derived **wt2** (Table 1). Comparing the affinities of **1** and the chimeric peptide **2** toward ENAH EVH1 reveals that truncation of the flanking residues significantly contributes to the binding with about −8 kJ/mol. Binding studies with selectively truncated peptides **2ΔN** or **2ΔC** lacking either the N- or C-terminal flanking residues indicated that the C-terminal TEDEL−NH₂ portion was almost solely responsible for the observed affinity loss with respect to **2** (Table 1). The finding confirmed a previous presumption that the terminal amino acids Glu-Leu of TEDEL represent an additional binding epitope of VASP EVH1 (49). Noteworthy, earlier attempts to gain structural insights into the binding mechanism of C-terminally elongated peptides had failed (50), and docking studies are unreliable since the protein surface on the C-terminal side of the binding groove is nearly featureless. Therefore, we first focused on elucidating the structural details of the TEDEL interaction with the protein surface as a precondition for the design of analogs of the parent inhibitor **1** with improved affinity.

Crystal Structures of ENAH EVH1 in Complex with TEDEL-Containing Chimeras. Initial attempts to cocrystallize the N-terminally truncated wild-type 10-mer Ac–¹FPPPPTEDEL−NH₂ with ENAH EVH1 failed. However, replacing ¹Phe by Trp or 2-Cl-Phe and/or substituting ⁴PP by ProM-1 increased the affinity and yielded crystal structures with resolution limits up to 1.0 Å (*SI Appendix*, Fig. S4*A*). The structures unambiguously revealed that TEDEL adopts an α-helical loop conformation exposing acidic residues to the solvent and positioning the terminal ⁹EL over the protein surface in close vicinity to the core recognition motif (Fig. 2*A* and *SI Appendix*, Figs. S4–S8).

A closer analysis of the interaction between the TEDEL loop and the protein surface shows that the carboxylate group of ⁹Glu forms a hydrogen bond to the backbone amide of Trp23 (W23NH), thereby displacing a highly conserved water molecule found in every complex structure of inhibitors missing TEDEL (Fig. 2*B*). The helical loop conformation suggested that the sidechain length of ⁹Glu is needed to properly place the carboxylate group over W23NH. Consequently, mutating ⁹Glu to ⁹Asp decreased the binding affinity by a factor of 3 (*SI Appendix*, Fig. S4*C*). The polar interaction site of ⁹Glu is separated by 8 Å from a nonpolar patch that contacts the terminal ¹⁰Leu. The patch is mainly defined by Met14 and extends toward the hydrophobic binding groove, where Phe77 contacts ⁵Pro with high specificity (*SI Appendix*, Fig. S3). Due to the helix pitch of TEDEL, a long hydrophobic amino acid is needed to contact Met14 (Fig. 2*C*). Consequently, mutating ¹⁰Leu to ¹⁰Ala results in nearly three times weaker binding (*SI Appendix*, Fig. S4*C*). The ligand sidechains ⁵Pro and ¹⁰Leu shield the hydrophobic interaction site entirely from solvent (*SI Appendix*, Fig. S8). The coverage area of the last two prolines ⁴Pro and ⁵Pro can be enlarged by replacing them with ProM-1 which leads to a gain of −3.5 kJ/mol of binding energy (*SI Appendix*, Tables S7 and S8 and Fig. S11). Interestingly, ProM-1 and TEDEL appear to be two independent affinity-driving elements as the TEDEL conformation remains unaltered in ProM-containing chimeras (*SI Appendix*, Fig. S4*B*) and TEDEL-elongated inhibitors still bound canonically to the binding groove (Fig. 2*D*).

Having analyzed the contribution of the terminal ⁹EL residues by means of high-resolution crystal structures of TEDEL-containing ligands in complex with ENAH EVH1, the next task was to exploit this knowledge in the design of improved analogs of the parent inhibitor **1**. Specifically, we sought to modify the C-terminal ProM-1 unit to also address the additional, so far uncovered, polar and nonpolar interaction sites.

Table 1. Affinities of various inhibitors toward ENAH EVH1 determined by fluorescence titration

	Ligand composition	K_d, μM	ΔG, kJ/mol
wt1	Ac–FPPPP–OEt	153 (8)	−21.9 (0.1)
wt2	Ac–SFEFPPPPTEDEL–NH$_2$	13.0 (0.6)	−27.9 (0.1)
1	Ac–[2-Cl-Phe][ProM-2][ProM-1]–OEt	4.1 (0.3)	−30.8 (0.2)
1a	Ac–[2-Cl-Phe][ProM-2][ProM-1]–OMe	4.4 (0.7)	−30.6 (0.4)
1b	Ac–[2-Cl-Phe][ProM-2][ProM-1]–OH	2.3 (0.2)	−32.2 (0.2)
2	Ac–SFE[2-Cl-Phe][ProM-2][ProM-1]TEDEL–NH$_2$	0.15 (0.02)	−38.9 (0.2)
2ΔN	Ac–[2-Cl-Phe][ProM-2][ProM-1]TEDEL–NH$_2$	0.33 (0.04)	−37.0 (0.3)
2ΔC	Ac–SFE[2-Cl-Phe][ProM-2][ProM-1]–OEt	2.9 (0.2)	−31.6 (0.1)
3a	Ac–[2-Cl-Phe][ProM-2][ProM-12]–OMe	15 (1)	−27.6 (0.2)
3b	Ac–[2-Cl-Phe][ProM-2][ProM-12]–OH	13.5 (0.4)	−27.8 (0.1)
4a	Ac–[2-Cl-Phe][ProM-2][ProM-15]–OMe	0.47 (0.03)	−36.1 (0.1)
4b	Ac–[2-Cl-Phe][ProM-2][ProM-15]–OH	0.32 (0.04)	−37.0 (0.3)
5a	Ac–[2-Cl-Phe][ProM-2][ProM-17]–OMe	0.53 (0.09)	−35.8 (0.4)
6	Ac–[2-Cl-Phe][ProM-2][ProM-9]–OEt	0.38 (0.05)	−36.6 (0.3)
6b	Ac–[2-Cl-Phe][ProM-2][ProM-9]–OH	0.12 (0.02)	−39.5 (0.3)
6c	Ac–[2-Cl-Phe]PP[ProM-9]–OH	0.23 (0.05)	−37.9 (0.5)
7	Ac–[2-Cl-Phe][ProM-2][ProM-13]–OEt	0.12 (0.01)	−39.5 (0.3)

K_d and ΔG values are given with the standard errors in parentheses.

Inhibitors 3, 4, and 5 Access the Polar Hot Spot. To mimic the polar interaction of [9]Glu with W23NH, docking studies suggested that the configurational inversion of the C-terminal carboxyl substituent could improve binding through directly contacting the H$_2$O bound to W23NH (Fig. 2B). We therefore synthesized ProM-12 (*epi*-ProM-1) and the corresponding inhibitors **3a** and **3b** (methyl ester or free acid; Table 1) with the terminal carboxylic group now pointing toward the protein surface. Even though these inhibitors established a 2.7-Å-long H-bond to the bound water molecules as intended (Fig. 3 *A* and *B*), both inhibitors **3a** and **3b** lost significant affinity relative to their parent congeners **1a** and **1b** (Table 1). This decreased affinity is reflected in the complex structures of **3a** and **3b** with resolution limits up to 1.42 Å by a detachment of the modified C-terminal part of the inhibitors from the hydrophobic protein surface locally defined by the Trp23 and Phe77 sidechains (Fig. 3B).

To address the polar hot spot while keeping the hydrophobic contact in the C-terminal area undisturbed, docking studies suggested to formally open the C-terminal pyrrolidine ring of inhibitor **1** or **3**. Such a modification opened the possibility to probe the underlying hydrophobic binding groove with different moieties (ProM-15 and ProM-17; Fig. 1B) (47). The resulting less rigid inhibitors **4a** and **5a** showed a greatly improved affinity toward ENAH EVH1 by −5.5 kJ/mol compared to **1a**, thereby nearly restoring the binding energy of the TEDEL-containing chimera **2ΔN** (Table 1). The complex structures of **4a** and **4b** with resolution limits up to 1.1 Å confirmed that the "ethyl finger" of ProM-15 indeed established the contact with the hydrophobic binding groove while the ester function maintained a 2.7-Å-long H-bond contact with the water bound to W23NH (Fig. 3C and *SI Appendix*, Fig. S9). Even though inhibitor **5a** was expected to further enhance affinity by covering the hydrophobic area with an isobutyl group, it bound just as well as **4a**. The structure of **5a** in complex with ENAH EVH1 at a resolution limit of 0.78 Å revealed the sterically more demanding ProM-17 scaffold being a bit too bulky, causing the inhibitor to be N-terminally shifted away from the ideal position (Fig. 3 *C* and *D*). Consequently, the H-bond contact to the W23NH-bound water widened to 3.0 Å. Due to the lack of affinity gain, inhibitor **5a** was not investigated further in cellular assays.

Inhibitors 6 and 7 Cover the Hydrophobic Patch. The results obtained with the ProM-12–, ProM-15–, and ProM-17–derived inhibitors emphasize the particular importance to properly cover the hydrophobic binding site spanned by Phe77 and Met14 rather than accessing the H$_2$O bound to W23NH (Fig. 3D). As indicated by docking studies we envisioned that this hydrophobic hot spot could be specifically accessed by equipping **1** with an
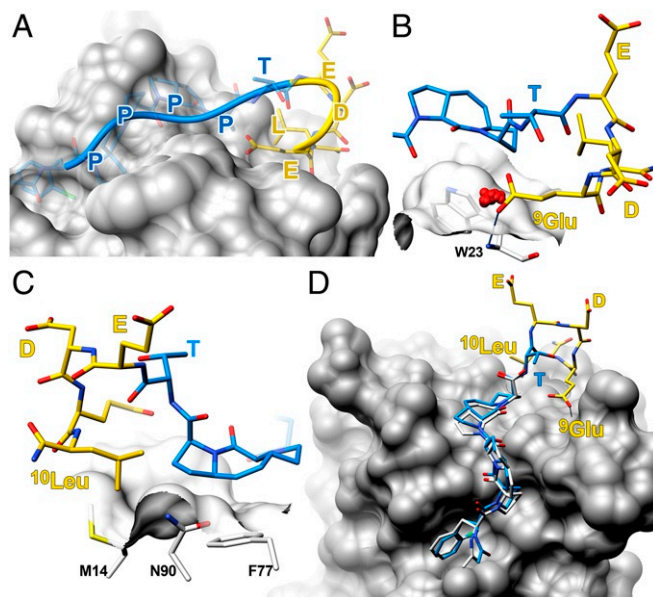

Fig. 2. Crystal structure of chimera **2ΔN** in complex with ENAH EVH1 reveals the TEDEL loop binding close to the main binding groove through polar and nonpolar interactions. (*A*) Interaction sites of terminal EL. **2ΔN** is displayed as ribbon and transparent sticks, color coded by a secondary structure element: PPII (blue) and α-helix (yellow). (*B*) The backbone amide nitrogen of W23 is contacted by either [9]Glu or a conserved water molecule (superposition of 19 H$_2$O from 12 asymmetric units). (*C*) The hydrophobic site provided by M14 and F77 is reachable only by a long aliphatic amino acid such as [10]Leu. (*D*) Superposition of inhibitor **1b** (white) and **2ΔN** (blue-yellow). View along the main binding groove reveals only minor ligand rearrangements.
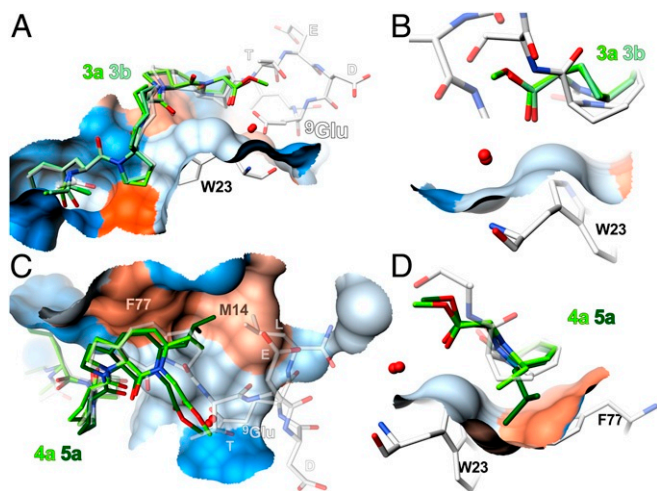
Fig. 3. Crystal structures of ENAH EVH1 in complex with ProM-12–, ProM-15–, and ProM-17–containing inhibitors. The solvent-accessible surface of ENAH EVH1 is color coded by hydrophobicity (blue-white-red for hydrophilic–hydrophobic). (*A*) Superposition of 2ΔN (white) and the ProM-12–containing inhibitors **3a** and **3b** (green). (*B*) Detailed view highlighting the disturbed contact of the carboxyl substituent of **3a** and **3b** to their respective bound water molecules (red spheres) associated to an unfavorable detachment from the W23 sidechain in comparison to 2ΔN (white). (*C*) Superposition of 2ΔN (white) with inhibitors **4a** (light green) and **5a** (dark green). (*D*) Detailed view illustrating the capability of ProM-15 (**4a**) and ProM-17 (**5a**) to address the hydrophobic groove while maintaining contact to their respective bound water molecules (red spheres).

additional alkyl substituent at the C-terminal pyrrolidine ring. For this reason the alkylated derivatives of ProM-1, i.e., ProM-9 and ProM-13 (Fig. 1*B*), were synthesized (46) and used to prepare the desired inhibitors **6** and **7** (Table 1). Affinity measurements then showed that both inhibitors outperformed **1** substantially and lowered the K_d to 380 nM (**6**) and 120 nM (**7**). Noteworthy, inhibitor **7** gained −8.7 kJ/mol relative to **1** and bound equally strong as the untruncated chimera **2**. Thus, by calculated introduction of a single ethyl substituent we succeeded in restoring the entire binding energy of eight flanking amino acid residues and in coming up with a potent 734-Da inhibitor binding canonically to all Ena/VASP EVH1 domains (*SI Appendix*, Table S9). The formal alkylation of inhibitor **1** increased its molecular weight by less than 4% and improved the ligand efficiency (51) (*SI Appendix*, Table S9).

High-resolution crystal structures of ENAH EVH1 in complex with inhibitors **6b** and **7** at 1.02 Å resolution confirmed that the modified scaffolds indeed accessed the hydrophobic hot spot as intended (Fig. 4 *A* and *B* and *SI Appendix*, Fig. S10). Superposition with inhibitors 2ΔN, **1b**, or **4a** highlighted that both optimized scaffolds showed little conformational bias and only marginal displacements. Thus, the observed affinity boost from **1** (K_d 4.1 μM) to **7** (K_d 0.12 μM) clearly results from properly covering Trp23, Met14, and Phe77 by the additional ethyl substituent of ProM-13 (Fig. 4 *C* and *D*).

The Optimized Inhibitors Are Selective and Compete with Natural Binding Partners of Ena/VASP. We first tested whether the optimized inhibitors retained specificity toward Ena/VASP EVH1 compared to other proline-rich motif-recognizing proteins. We used sensible ^{1}H-^{15}N heteronuclear single quantum coherence (HSQC) NMR experiments and assigned peak perturbation trajectories to assess the binding affinities of **1**, **4a**, and **7** also against Fyn SH3, Profilin, and Yap1 WW1 (Fig. 5*A*). This in turn allowed additional structural insights into the binding mode to off-target proteins and confirmed that all inhibitors were recognized by the

canonic interaction sites of Fyn SH3, Profilin, and Yap1 WW1, corroborating the ability of ProM scaffolds to mimic PPII secondary structure elements (*SI Appendix*, Figs. S13 and S21). At the same time, all inhibitors bound with drastically decreased affinity to the off-target proteins compared to ENAH EVH1, and this decrease was more prominent for the optimized inhibitors **4a** and **7** (*SI Appendix*, Table S10), suggesting that in silico optimization not only yielded highly desirable affinity boosts but also increased the selectivity for Ena/VASP EVH1. The specificity seen in HSQC experiments also held in a more complex environment such as the Jurkat cell lysate. Inhibitors **1**, **4a**, **6**, and **7** were not competing with the natural binding partner ADAP (52) for Fyn SH3, while the synthetic peptide Ac–RPLPPPLP–NH$_2$ (53) with a measured K_d of 8.2 μM displaced ADAP from bead-bound GST-Fyn SH3 at the same concentration (in vitro pulldown; *SI Appendix*, Fig. S22).

To probe whether the developed compounds also exhibit the expected biological activity, we investigated their effect on triple-negative (estrogen receptor-, progesterone receptor-, and HER2-negative) breast cancer cells (MDA–MB–231), which represent a major therapeutic challenge (54). At first we assessed the efficiency of **7** to compete with known binding partners for Ena/VASP EVH1 by performing in vitro pulldown experiments with MDA–MB–231 cell lysate to find that the initial (**1**) and the structure-optimized (**7**) inhibitor were able to compete for ENAH EVH1 with RAPH1 (16), RIAM (34), and Zyxin (55) in a concentration-dependent manner (Fig. 5*B*). Analysis of the Western blot revealed that the half-maximal inhibitory concentration (IC50) of **7** was 18 times smaller than that of **1** (mean IC50 0.67 μM vs. 12 μM, $P < 0.0002$).

Optimized Inhibitors Potently Inhibit Ena/VASP-Mediated Breast Cancer Cell Invasion. As Ena/VASP proteins are centrally involved in the formation of protrusive structures during cell migration (16, 18) and degradation of extracellular matrix (56), we expected that inhibiting their interaction with natural binding partners might affect the invasiveness of cancer cells. Indeed, incubating MDA–MB–231 with inhibitors **1**, **4a**, **6**, and **7** reduced chemotaxis along a fetal bovine serum (FBS) gradient in a
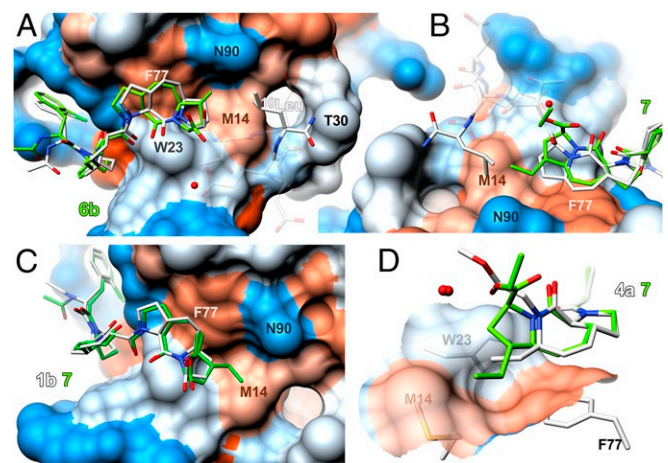

Fig. 4. Crystal structures of ENAH EVH1 in complex with ProM-9– and ProM-13–containing inhibitors. The solvent-accessible surface of ENAH EVH1 is color coded by hydrophobicity (blue-white-red for hydrophilic–hydrophobic). (*A* and *B*) Superposition of inhibitors **6b** and **7** with 2ΔN (white) shows how the additional alkylation at the C-terminal pyrrolidine ring accesses the apolar hot spot addressed by ^{10}Leu in 2ΔN. (*C*) Superposition of inhibitors **7** and **1b** (white) reveals little conformational bias and marginal displacements. (*D*) Superposition of inhibitors **7** and **4a** highlights the coverage of F77 and W23.
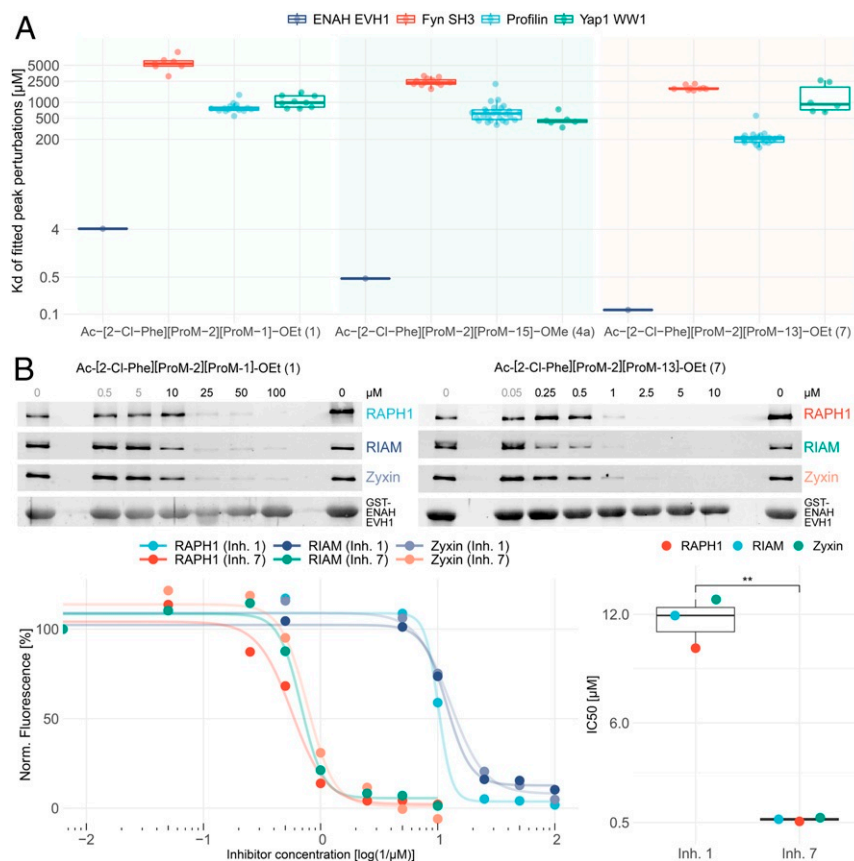
Fig. 5. In vitro studies with the initial and optimized inhibitors. (*A*) The ^{1}H-^{15}N HSQC titration experiments to assess the off-target specificity of **1**, **4a**, and **7**. Each inhibitor was tested against a selection of domains recognizing proline-rich segments (Fyn SH3, Profilin, and Yap1 WW) and peak perturbations farther than 0.1 ppm were taken into account. Plotted are fitted K_d on a logarithmic scale, together with the according affinities for ENAH EVH1 taken from Table 1. (*B*) Pulldown experiments and fluorescence-based analysis of GST-tagged ENAH EVH1 from MDA–MB–231 cell lysates treated with **1** or **7**. Natural binding partners RAPH1, RIAM, and Zyxin are displaced by the inhibitors from ENAH EVH1 in a concentration-dependent manner with different IC50 values ($P = 1.6e-4$).

dose-dependent manner (Fig. 6*A* and *SI Appendix*, Fig. S23). The calculated IC50 values confirmed that optimized inhibitors exhibit a superior potency compared to **1** (Fig. 6 *A*, *Right*; mean IC50 **1**, 88 μM; **4a**, 53 μM; **6**, 24 μM; and **7**, 26 μM). The increased potency of **7** was also confirmed in a Boyden chamber invasion assay (*SI Appendix*, Fig. S24). To exclude possible toxic effects, we tested inhibitors **1**, **4a**, **6**, and **7** in MDA–MB–231 but also Ena/VASP triple-knockout mouse fibroblastic MV^{D7} and Ena/VASP triple-knockout mouse melanoma cell lines. None of the cell lines showed toxic effects at 180 μM (*SI Appendix*, Fig. S25).

To determine whether the increased potency seen for inhibitors **4a**, **6**, and **7** also holds in vivo, we investigated their effect on the extravasation of MDA–MB–231 cells in transgenic zebrafish embryos (*fli:*EGFP) (57) (Fig. 6*A*). Simulating the late stage of the metastatic cascade, we measured the ability of MDA–MB–231 cells to extravasate into the avascular collagen matrix-rich tailfin (58). Counting the number of cells that have extravasated and invaded the tailfin tissue, we could indeed verify that inhibition of the Ena/VASP-mediated processes caused pronounced antiinvasive effects (Fig. 6*B*). In contrast to the initial inhibitor **1**, which at 1 μM concentration did not show any effect compared to zebrafish treated with phosphate-buffered saline (PBS) ($P > 0.2$), the structure-optimized inhibitors significantly reduced cancer cell extravasation (**4a** and **7**, $P < 0.0001$; **6**, $P < 0.005$). Surprisingly, the weaker binding inhibitor **4a** exhibited a similarly strong in vivo activity to that of **7** probably due to different secondary properties such as cell permeability. These

data indicate that the structure-based optimization of our EVH1 inhibitors (Fig. 1*B*) not only resulted in a gain of binding affinity but also opened options to fine-tune their pharmacological properties.

Discussion

Based on recent evidence that Ena/VASP is a critical factor in metastatic cancer progression, we targeted its EVH1 adapter domain which recognizes proline-rich segments on a shallow, rigidly shaped, and nearly featureless protein surface. The challenge to develop a small molecule inhibitor for this seemingly "undruggable" protein–protein interaction was successfully met by combining X-ray crystallography, in silico design, and chemical synthesis of modular inhibitors displaying a preorganized PPII secondary structure. To extend our toolbox of conformationally defined proline-derived synthetic scaffolds (ProMs) we first identified two affinity-driving hot spots on the surface of ENAH EVH1 by characterizing the binding mode of TEDEL-elongated ligands. In a second step we then specifically modified our initial inhibitor **1** to exploit these interaction sites: The ProM-15– and ProM-17–derived inhibitors **4a** and **5a**, designed to contact the discovered polar hot spot, showed an impressive gain of affinity (K_d of 470 and 530 nM, respectively). These compounds were even surpassed by the ProM-9– and ProM-13–derived inhibitors **6** and **7**, designed to cover a hydrophobic patch, the latter binding to ENAH EVH1 with a K_d of 120 nM. Thus, by calculated introduction of a single ethyl substituent close to the C terminus of **1** we could gain as much binding
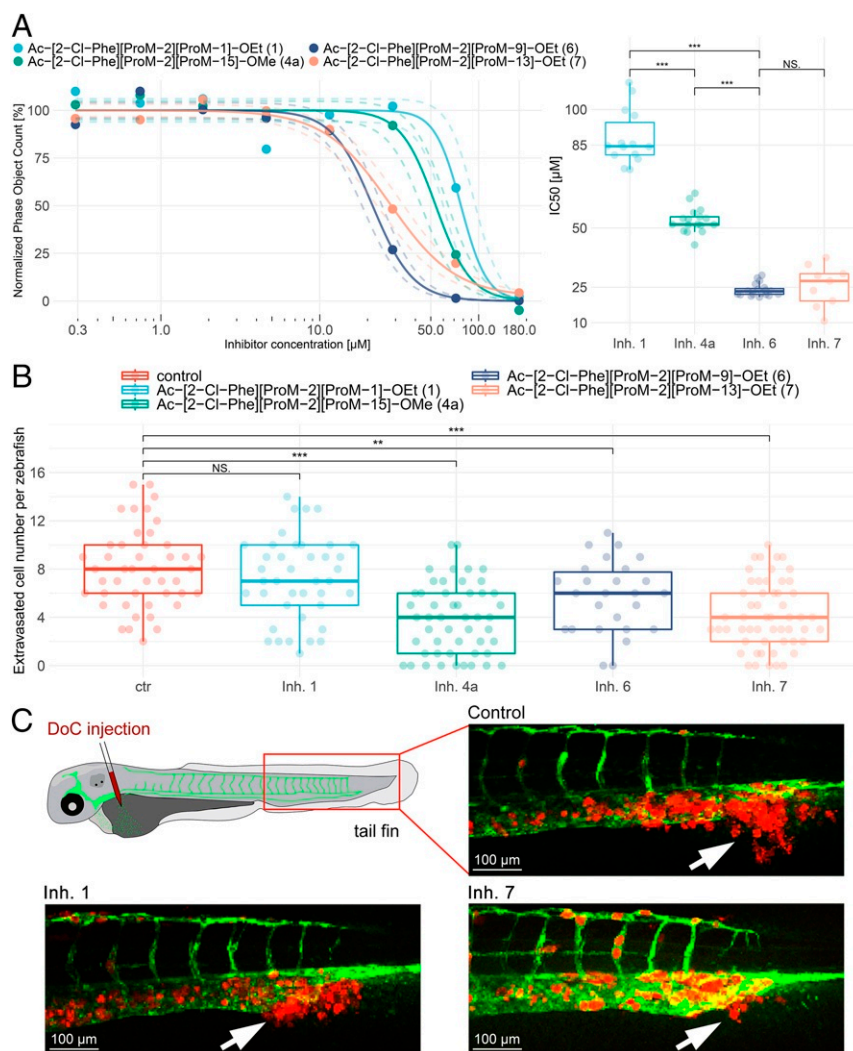
Fig. 6. Cellular and in vivo studies with the initial and optimized inhibitors. (*A*) IncuCyte chemotaxis assay with inhibitor-treated MDA–MB–231. (*Left*) Invasion is inhibited in a dose-dependent manner (representative phase object count, normalized to fitted IC50 curves with 3σ dashed line). (*Right*) IC50s were calculated during linear phase object signal increase of the assay and are plotted as a group. (*B*) MDA–MB–231 cancer cells extravasation in zebrafish treated with PBS (control) or inhibitors **1**, **4a**, **6**, or **7** at 1 μM concentration. (*C*) Representative fluorescence images of zebrafish embryos taken on day 5. MDA–MB–231 (red) extravasate into the avascular tailfin (white arrows).

energy as contributed by the eight flanking amino acid residues of the chimeric ligand **2**. Furthermore, we showed that the structure-optimized inhibitors compete with known Ena/VASP interaction partners and exhibit increased selectivity for the EVH1 domain compared to related proline-rich recognizing proteins, both in vitro and in a complex environment such as the Jurkat cell lysate. All optimized inhibitors **4a**, **6**, and **7** interfere with the invasion of MDA–MB–231 cells with increased potency compared to the initial inhibitor **1**. Finally, we could demonstrate the ability of the optimized compounds to inhibit cancer cell extravasation in vivo in a zebrafish model at 1 μM concentration. This way, we proved that synthetic Ena/VASP EVH1 inhibitors exhibit biological activity also beyond cellular assays.

Materials and Methods

Protein Purification. Ena/VASP EVH1 domains were expressed as GST-fusion proteins in *E. coli* BL21(DE3) grown in 2YT medium overnight. After sonication and centrifugation the soluble fraction was loaded on a glutathione Sepharose matrix and eluted with GSH. GST was cleaved overnight with thrombin and loaded on an SP Sepharose ion exchange column and rebuffered by passing over a HiLoad 16/60 Superdex 75 size exclusion column.

Crystallization. Crystals were obtained by sitting vapor diffusion using microseeding and 8 to 26 mg/mL ENAH EVH1 at 293 to 300 K with different ligand excess. All structures were solved by molecular replacement, refined by the PHENIX program suite, and deposited at the Protein Data Base databank. Diffraction and refinement statistics and the accession codes are listed in *SI Appendix*, Tables S1–S6. Complex structures were superposed by rigid body match using the five atomic positions W23NE, W23N, F77CG, Y16CG, and Q79CD and images were rendered in Chimera.

Binding Studies. Dissociation constants were determined via fluorescence titration or isothermal titration calorimetry at 298 K in 40 mM sodium phosphate, pH 7.3, 100 mM NaCl, and 2 mM TCEP. HSQC NMR spectra were recorded on a Bruker AV600 at 300 K with 16 scans, data size 1,024 (^{1}H) $\times$ 256 (^{15}N), and peak perturbation trajectories were tracked in Sparky.

Pulldown Assay. GST-ENAH EVH1 or GST-Fyn SH3 were immobilized on glutathione Sepharose 4B beads using MDA–MB–231 or Jurkat cell lysate. Displacement of natural binding partners was achieved by adding inhibitors to the lysate incubating overnight on beads at 4 °C. The Western blot with target-specific antibodies was read out by a fluorescence-based secondary antibody on an infrared scanner.

IncuCyte Assay. Migration of 2,000 cells per well was monitored by the IncuCyte S3 live cell imaging system over a gradient of 0.25% FBS (insert) to 1% FBS (lower chamber) in Dulbecco's Modified Eagle Medium (DMEM) high-glucose medium, with the inhibitors supplied in both chambers. The experiment was set up as a triplet for the inhibitor concentrations and quadruplets for the positive (PBS) and negative controls (20 μM PI3K inhibitor LY294002). Raw data were averaged and processed with a script written in R language.

Zebrafish Assay. mCherry-labeled MDA–MB–231 were injected into the duct of curvier of transgenic zebrafish embryos (*fli:EGFP*) and administrated with corresponding inhibitor treatment. Zebrafish embryos were maintained at 34 °C and the numbers of MDA–MB–231 cells that extravasated individually from circulation into the collagen fibers of the tail fin were counted 5 d postinjection.

Data and Code Availability. All study data are included in this article and *SI Appendix*.

1. I. J. Fidler, S. Paget, The pathogenesis of cancer metastasis: The 'seed and soil' hypothesis revisited. *Nat. Rev. Cancer* **3**, 453–458 (2003).
2. P. Friedl, S. Alexander, Cancer invasion and the microenvironment: Plasticity and reciprocity. *Cell* **147**, 992–1009 (2011).
3. L. Blanchoin, R. Boujemaa-Paterski, C. Sykes, J. Plastino, Actin dynamics, architecture, and mechanics in cell motility. *Physiol. Rev.* **94**, 235–263 (2014).
4. M. Vicente-Manzanares, C. K. Choi, A. R. Horwitz, Integrins in cell migration–the actin connection. *J. Cell Sci.* **122**, 199–206 (2009).
5. C. Albiges-Rizo, O. Destaing, B. Fourcade, E. Planus, M. R. Block, Actin machinery and mechanosensitivity in invadopodia, podosomes and focal adhesions. *J. Cell Sci.* **122**, 3037–3049 (2009).
6. J. S. Desgrosellier, D. A. Cheresh, Integrins in cancer: Biological implications and therapeutic opportunities. *Nat. Rev. Cancer* **10**, 9–22 (2010).
7. M. Campone *et al.*, Phase II study of single-agent bosutinib, a src/abl tyrosine kinase inhibitor, in patients with locally advanced or metastatic breast cancer pretreated with chemotherapy. *Ann. Oncol.* **23**, 610–617 (2012).
8. B. Y. Lee, P. Timpson, L. G. Horvath, R. J. Daly, FAK signaling in human cancer as a target for therapeutics. *Pharmacol. Ther.* **146**, 132–149 (2015).
9. C. Davis *et al.*, Availability of evidence of benefits on overall survival and quality of life of cancer drugs approved by European medicines agency: Retrospective cohort study of drug approvals 2009-13. *BMJ* **359**, j4530 (2017).
10. W. P. Mason, End of the road: Confounding results of the core trial terminate the arduous journey of cilengitide for glioblastoma. *Neuro-oncology* **17**, 634–635 (2015).
11. R. Katayama *et al.*, Mechanisms of acquired crizotinib resistance in alk-rearranged lung cancers. *Sci. Transl. Med.* **4**, 120ra17 (2012).
12. L. Finn, S. N. Markovic, R. W. Joseph, Therapy for metastatic melanoma: The past, present, and future. *BMC Med.* **10**, 23 (2012).
13. N. P. Shah *et al.*, Clinical features of pulmonary arterial hypertension in patients receiving dasatinib. *Am. J. Hematol.* **90**, 1060–1064 (2015).
14. P. S. Steeg, Targeting metastasis. *Nat. Rev. Cancer* **16**, 201–218 (2016).
15. B. W. Stewart, *World Cancer Report 2014*, B. W. Stewart, C. P. Wild, Eds. (IARC Non-serial Publication, World Health Organization, International Agency for Research on Cancer, Geneva, Switzerland, 2016).
16. G. Carmona *et al.*, Lamellipodin promotes invasive 3D cancer cell migration via regulated interactions with Ena/VASP and SCAR/WAVE. *Oncogene* **35**, 5155–5169 (2016).
17. C. Bilancia *et al.*, Enabled negatively regulates diaphanous-driven actin dynamics in vitro and in vivo. *Dev. Cell* **28**, 394–408 (2014).
18. S. Havrylenko *et al.*, Wave binds Ena/VASP for enhanced Arp2/3 complex-based actin assembly. *Mol. Biol. Cell* **26**, 55–65 (2015).
19. X. J. Chen *et al.*, Ena/VASP proteins cooperate with the wave complex to regulate the actin cytoskeleton. *Dev. Cell* **30**, 569–584 (2014).
20. M. Barzik, L. M. McClain, S. L. Gupton, F. B. Gertler, Ena/VASP regulates mdia2-initiated filopodial length, dynamics, and function. *Mol. Biol. Cell* **25**, 2604–2619 (2014).
21. P. Beli, D. Mascheroni, D. Xu, M. Innocenti, WAVE and Arp2/3 jointly inhibit filopodium formation by entering into a complex with mDia2. *Nat. Cell Biol.* **10**, 849–857 (2008).
22. F. B. Gertler, K. Niebuhr, M. Reinhard, J. Wehland, P. Soriano, Mena, a relative of VASP and Drosophila enabled, is implicated in the control of microfilament dynamics. *Cell* **87**, 227–239 (1996).
23. F. Di Modugno *et al.*, The cytoskeleton regulatory protein hmena (enah) is overexpressed in human benign breast lesions with high risk of transformation and human epidermal growth factor receptor-2-positive/hormonal receptor-negative tumors. *Clin. Cancer Res.* **12**, 1470–1478 (2006).
24. E. T. Roussos *et al.*, Mena deficiency delays tumor progression and decreases metastasis in polyoma middle-t transgenic mouse mammary tumors. *Breast Cancer Res.* **12**, R101 (2010).
25. R. L. Klemke, Trespassing cancer cells: 'fingerprinting' invasive protrusions reveals metastatic culprits. *Curr. Opin. Cell Biol.* **24**, 662–669 (2012).
26. L. Dertsiz *et al.*, Differential expression of VASP in normal lung tissue and lung adenocarcinomas. *Thorax* **60**, 576–581 (2005).
27. L. D. Hu, H. F. Zou, S. X. Zhan, K. M. Cao, EVL (Ena/VASP-like) expression is up-regulated in human breast cancer and its relative expression level is correlated with clinical stages. *Oncol. Rep.* **19**, 1015–1020 (2008).
28. F. Di Modugno *et al.*, The cooperation between hMena overexpression and HER2 signalling in breast cancer. *PLoS One* **5**, e15852 (2010).
29. P. Tucker, I. Evans, W. Wood, Ena drives invasive macrophage migration in Drosophila embryos. *Dis. Model. Mech.* **4**, 126–134 (2011).
30. U. Philippar *et al.*, A Mena invasion isoform potentiates EGF-induced carcinoma cell invasion and metastasis. *Dev. Cell* **15**, 813–828 (2008).
31. C. Bachmann, L. Fischer, U. Walter, M. Reinhard, The evh2 domain of the vasodilator-stimulated phosphoprotein mediates tetramerization, f-actin binding, and actin bundle formation. *J. Biol. Chem.* **274**, 23549–23557 (1999).
32. J. E. Bear *et al.*, Antagonism between Ena/VASP proteins and actin filament capping regulates fibroblast motility. *Cell* **109**, 509–521 (2002).
33. J. E. Bear *et al.*, Negative regulation of fibroblast motility by Ena/VASP proteins. *Cell* **101**, 717–728 (2000).
34. E. Lafuente *et al.*, Riam, an Ena/VASP and profilin ligand, interacts with Rap1-GTP and mediates Rap1-induced adhesion. *Dev. Cell* **7**, 585–595 (2004).
35. M. Krause *et al.*, Lamellipodin, an Ena/VASP ligand, is implicated in the regulation of lamellipodial dynamics. *Dev. Cell* **7**, 571–583 (2004).
36. D. S. Zuzga *et al.*, Phosphorylation of vasodilator-stimulated phosphoprotein Ser239 suppresses filopodia and invadopodia in colon cancer. *Int. J. Cancer* **130**, 2539–2548 (2012).
37. H. Paz, N. Pathak, J. Yang, Invading one step at a time: The role of invadopodia in tumor metastasis. *Oncogene* **33**, 4193–4202 (2014).
38. L. J. Ball, T. Jarchau, H. Oschkinat, U. Walter, EVH1 domains: Structure, function and interactions. *FEBS* **513**, 45–52 (2002).
39. D. E. Scott, A. R. Bayly, C. Abell, J. Skidmore, Small molecules, big targets: Drug discovery faces the protein-protein interaction challenge. *Nat. Rev. Drug Discov.* **15**, 533–550 (2016).
40. R. Opitz *et al.*, A modular toolkit to inhibit proline-rich motif-mediated protein-protein interactions. *Proc. Natl. Acad. Sci. U.S.A.* **112**, 5011–5016 (2015).
41. J. Zaminer *et al.*, Addressing protein-protein interactions with small molecules: A pro-pro dipeptide mimic with a PPII helix conformation as a module for the synthesis of prd-binding ligands. *Angew Chem. Int. Ed. Engl.* **49**, 7111–7115 (2010).
42. V. Hack *et al.*, Efficient α-helix induction in a linear peptide chain by n-capping with a bridged-tricyclic diproline analogue. *Angew Chem. Int. Ed. Engl.* **52**, 9539–9543 (2013).
43. C. Reuter, P. Huy, J. Neudörfl, R. Kühne, H. G. Schmalz, Exercises in pyrrolidine chemistry: Gram scale synthesis of a pro-pro dipeptide mimetic with a polyproline type II helix conformation. *Chemistry* **17**, 12037–12044 (2011).
44. C. Reuter *et al.*, Stereoselective synthesis of proline-derived dipeptide scaffolds (ProM-3 and ProM-7) rigidified in a PPII helix conformation. *Eur. J. Org. Chem.* **13**, 2664–2667 (2014).
45. C. Reuter *et al.*, Design and stereoselective synthesis of prom-2: A spirocyclic diproline mimetic with polyproline type II (PPII) helix conformation. *Chem. Eur. J.* **21**, 8464–8470 (2015).
46. S. Chiha *et al.*, Design and synthesis of building blocks for PPII-helix secondary-structure mimetics: A stereoselective entry to 4-substituted 5-vinylprolines. *Eur. J. Org. Chem.* **4**, 455–460 (2018).
47. S. Dohmen *et al.*, Pd-catalyzed asymmetric N-allylation of amino acid esters with exceptional levels of catalyst control: Stereo-divergent synthesis of ProM-15 and related bicyclic dipeptide mimetics. *Chem. Eur. J.* **26**, 3049–3053 (2020).
48. C. Kocks *et al.*, L. monocytogenes-induced actin assembly requires the actA gene product, a surface protein. *Cell* **68**, 521–531 (1992).
49. L. J. Ball *et al.*, Dual epitope recognition by the VASP EVH1 domain modulates polyproline ligand specificity and binding affinity. *EMBO J.* **19**, 4903–4914 (2000).
50. A. A. Fedorov, E. Fedorov, F. Gertler, S. C. Almo, Structure of EVH1, a novel proline-rich ligand-binding module involved in cytoskeletal dynamics and neural function. *Nat. Struct. Biol.* **6**, 661–665 (1999).
51. C. Abad-Zapatero, Ligand efficiency indices for effective drug discovery. *Expert Opin. Drug Discov.* **2**, 469–488 (2007).
52. A. J. da Silva *et al.*, Cloning of a novel T-cell protein FYB that binds FYN and SH2-domain-containing leukocyte protein 76 and modulates interleukin 2 production. *Proc. Natl. Acad. Sci. U.S.A.* **94**, 7493–7498 (1997).
53. A. B. Sparks, J. A. Quilliam, J. M. Thorn, C. J. Der, B. K. Kay, Identification and characterization of Src SH3 ligands from phage-displayed random peptide libraries. *J. Biol. Chem.* **269**, 23853–23856 (1994).
54. A. G. Waks, E. P. Winer, Breast cancer treatment: A review. *J. Am. Med. Assoc.* **321**, 288–300 (2019).
55. H. Hirata, H. Tatsumi, M. Sokabe, Zyxin emerges as a key player in the mechanotransduction at cell adhesive structures. *Commun. Integr. Biol.* **1**, 192–195 (2008).
56. H. Yamaguchi *et al.*, Molecular mechanisms of invadopodium formation: The role of the N-WASP-Arp2/3 complex pathway and cofilin. *J. Cell Biol.* **168**, 441–452 (2005).
57. J. Ren, S. Liu, C. Cui, P. Ten Dijke, Invasive behavior of human breast cancer cells in embryonic zebrafish. *J. Vis. Exp.* **122**, e55459 (2017).
58. Y. Drabsch, B. E. Snaar-Jagalska, P. Ten Dijke, Fish tales: The use of zebrafish xenograft human cancer cell models. *Histol. Histopathol.* **32**, 673–686 (2017).